Long-term (2000–2020) variability of in situ time series of Carbonyl Sulfide

C. Serio[1*], S. Montzka[2], G. Masiello[1], V. Carbone[3]

[1]Scuola di Ingegneria, Università degli studi della Basilicata, Potenza, Italy.

[2]NOAA Earth System Research Laboratory, Boulder, Colorado, USA

[3]Dipartimento di Fisica, Università della Calabria, Rende, Italy.

[*]Corresponding author address: Carmine Serio (carmine.serio@unibas.it)

Key Points:

- Atmospheric Carbonyl Sulfide is decreasing at NOAA network stations
- Time Series Analysis and Characteristic Scales encompassing one year to 8-10 years
- Empirical Mode Decomposition shows a reach wealth of frequencies, some compatible with Quasi Biennal Oscillation

Abstract

The monthly time series of carbonyl sulfide (OCS) atmospheric mole fractions measured at NOAA network stations (2000 to 2020) have been analyzed, and the long-term behaviour has been assessed based on the Empirical Mode Decomposition (EMD). EMD is a fully non-parametric analysis of frequency modes and trends in a given series and is based on the data alone. We have found that the OCS atmospheric mole fraction, after an increasing phase up to ~2015, with a temporary decline around 2009, is now decreasing at all stations, reflecting a recent imbalance in its total sources and losses. Our analysis has revealed a characteristic time scale for variation of 8-10 years. The variance associated with this long-term behaviour ranges from ∼15 to 40% of the total strength of the signal, depending on location. To our knowledge, this low-frequency mode is a novel result not assessed in previous studies. Apart from this complex long-term behaviour, the OCS time series show a strong annual cycle, which primarily results from summertime OCS uptake by vegetation. In addition, we have also found one more frequency of minor variance intensity in the measured mole fraction time-history, which corresponds to periods in the range of 2 to 3 years. This inter-annual variability of OCS may be linked to the Quasi-Biennial Oscillation or QBO.

.

Plain Language Summary

Carbonyl sulfide (OCS) is the most abundant sulfur-containing trace gas in the atmosphere and accounts for a significant part of sulfur in the stratospheric aerosol. OCS has recently emerged as a putative proxy for the terrestrial photosynthetic uptake of CO_2 because OCS and CO_2 have the same diffusion pathway into leaves. The OCS hydration reaction in this process is irreversible. For this reason, a better understanding of its time scales of variability can improve our knowledge of the carbon cycle. The study has analyzed OCS at 14 cooperative stations, which are distributed all around the world. We have found a characteristic time scale for 8-10 years variation. To our knowledge, this low-frequency mode is a novel result not assessed in previous studies. Apart from this complex long-term behaviour, the OCS time series show a robust yearly cycle, primarily from summertime OCS uptake by vegetation. Finally, we have also found one more frequency, which corresponds to periods in the range of 2 to 3 years. This inter-annual variability of OCS may be linked to the Quasi-Biennial Oscillation, which is an almost periodic oscillation of the winds of the equatorial stratosphere.

1. Introduction

The importance of carbonyl sulfide in the study of terrestrial vegetative ecosystems has clearly emerged in recent studies (Campbell et al., 2008, 2017; Maseyk et al., 2014; Montzka et al., 2007). OCS is the most abundant sulfur-containing trace gas in the atmosphere and accounts for a significant part of sulfur in the stratospheric aerosol (Brühl et al., 2012). Essential sources of OCS are natural, and among them, oceans, soils, and volcanic eruptions play a dominant role. Otherwise, anthropogenic sources have been recognized as secondary contributors: biomass burning and industrial activities (Campbell et al., 2008). The main sink of OCS has been identified as vegetation uptake, whose magnitude is also influenced by seasonal trends in terrestrial vegetative photosynthesis. Conversely, in the stratosphere, the photochemical loss is the prominent removal process, but at a substantially slower rate than vegetative uptake (Aydin et al., 2020; Berry et al., 2013; Glatthor et al., 2015; Kettle, 2002; Whelan et al., 2018).

Moreover, OCS has recently emerged as a putative proxy for the terrestrial photosynthetic uptake of CO_2 because OCS and CO_2 have the same diffusion pathway into leaves (Campbell et al., 2008; Montzka et al., 2007), and OCS hydration reaction in this process is irreversible. In addition to these earlier studies, more recent works (Berry et al., 2013; Campbell et al., 2015) have shown that carbonyl sulfide holds great promise for studies of carbon cycle processes because it is an atmospheric tracer of photosynthetic Gross Primary Production (GPP). According to (Berry et al., 2013; Campbell et al., 2015; Montzka et al., 2007), the uptake of OCS from the atmosphere is dominated by carbonic anhydrase (CA), an enzyme abundant in leaves that also catalyzes CO_2 hydration during photosynthesis. However, as a continuation of previous studies, it has been shown in (Ogée et al., 2016) that soils can also effectively exchange OCS with the atmosphere, which can complicate the retrieval of GPP from atmospheric budgets for some regions and scales. Some agricultural fields can take up large amounts of OCS from the atmosphere as soil microorganisms contain CA. OCS emissions from soils have been reported in agricultural fields or anoxic soils (Ogée et al., 2016). On a global scale, uptake by vegetation and soils account for more than 90% of the removal of OCS from the atmosphere, the remaining 10% being assigned to OH oxidation and transport to the stratosphere (Aydin et al., 2020; Berry et al., 2013; Glatthor et al., 2015; Kettle, 2002; Whelan et al., 2018).

Apart from seasonal variations, the OCS atmospheric mole fraction had remained relatively stable, e.g., within 7% (Montzka et al., 2007) for the period 2000-2005, when OCS routinely began measured at the 18 NOAA stations and aircraft profiling sites. Ice core and firm air measurements, e.g., (Aydin et al., 2020) and references therein, have been used to reconstruct atmospheric carbonyl sulfide's preindustrial and industrial history. The more recent atmospheric OCS abundance surveys use a panoply of complementary ground-based, airborne, and satellite observations, e.g., (Camy-Peyret et al., 2017; Krysztofiak et al., 2015; Lejeune et al., 2017; Montzka et al., 2007).

Almost all analyses of historical and contemporary data sets (Campbell et al., 2017) have been interpreted with models that simulate changes in OCS concentration according to changes in its global budget of natural and anthropogenic sources (from oceans and soils, from industry and biomass burning, respectively), and biogenic sinks (from plant photosynthesis and soils) as reviewed by (Whelan et al., 2018). Although anthropogenic emissions have exerted a dominant influence in driving secular atmospheric abundance changes since the 19^{th} century (Aydin et al., 2020; Campbell et al., 2015; Montzka et al., 2007) found that long-term changes in the observation-based OCS record were most consistent with simulations of climate and the carbon cycle that assume large growth in plant photosynthesis during the twentieth century. However, these analyses did not encompass the most recent trends in atmospheric OCS, e.g., since 2014-2015.

This study analyzes OCS measurements from the NOAA's global flask network, whose observing stations are spread around the globe but are more numerous in the North Hemisphere (NH), where anthropogenic sources are localized. A qualitative inspection of these data shows that the atmospheric OCS has entered a decline phase at all stations in recent years. Overall, we will show that a long-term behaviour with a characteristic time scale of ~8-10 years characterizes OCS time series from all sites analyzed in this study. However, over-imposed to this trend, there are cyclic behaviors with annual and inter-annual scales of variability.

The paper is organized as follows. Section 2 describes data and methods. Then, section 3 is devoted to presenting and discussing results. Finally, conclusions are taken in section 4.

2. Data and Methods

2.1. Data

For many years, OCS measurements from flasks have been obtained at approximately weekly intervals at 14 NOAA and cooperative stations (Montzka et al., 2007). The sampling process involves simultaneously pressurizing air into a pair of stainless steel or glass flasks that are subsequently shipped to the Boulder laboratory for analysis. Here we consider monthly mean mole fractions, and the data span different periods according to the station. The longest OCS time series at these sites extends from March 2000 to December 2020. Table 1 summarizes the basic information about the 14 stations, whereas Fig. 1 shows the position of the measurement stations around the globe.

Table 1. *NOAA stations whose OCS measurements from flasks have been analyzed in this study. The table also gives the percentage of missing data, as monthly means, for each time series. These gaps result from a lack of availability of flasks at a site and larger-than-acceptable differences in simultaneously filled flasks.*

Station	Code	Lat [°N]	Lon [°W]	Elevation [masl]	Time Interval endpoints	% Missing data
Alert, Nunavut, Canada	ALT	82.4508	62.5072	185	May 2000-October 2020	12.60
Point Barrow, USA	BRW	71.3230	156.6114	11	March 2000-December 2020	2.40
Cape Grim, Tasmania	CGO	-40.683	144.6900	94	February 2000-December 2020	3.60
Harvard Forest, USA	HFM	42.5378	72.1714	340	March 2000-December 2020	2.40
Cape Kumukahi, USA	KUM	19.7371	155.0116	0.30	March 2000-December 2020	0.80
Park Falls, USA	LEF	45.9451	90.2732	472	May 2000-December 2020	2.01
Mace Head, Ireland	MHD	53.3260	9.899	5.00	May. 2001-December 2020	7.60
Mauna Loa, USA	MLO	19.5362	155.5763	3397	March 2000-December2020	0.40
Niwot Ridge, USA	NWR	40.0531	105.5864	3523	March 2000-December 2020	3.20
Palmer Station, Antarctica	PSA	-64.7742	64.0527	10	May 2000-December 2020	14.50
Tutuila, American Samoa	SMO	-14.2474	170.5644	42	March 2000-December 2020	2.80
South Pole, Antarctica	SPO	-89.98	24.8	2810	May 2000-December 2020	11.29
Summit, Greenland	SUM	72.5962	38.422	3209	June 2004-December2020	5.03
Trinidad Head, USA	THD	41.0541	124.151	107	April 2002-December 2020	0.44

The time series can have occasional missing data (see also the last column in Tab. 1); when needed, gaps in the OCS sequences have been filled by cubic spline interpolation. An example is shown in Fig. 2. Because the sampling of OCS "events" is not the same at all stations and can vary at the same station, month-to-month, the event measurements are averaged to form monthly means. The analysis is then performed on these monthly time series. Also, we clarify that the gaps shown in Tab. 1 are assessed on the basis of the monthly time series. We also note that the uneven sample frequency at the same station adds a sampling noise, which the EMD methodology is capable of filtering out, as it will be shown further in the paper.

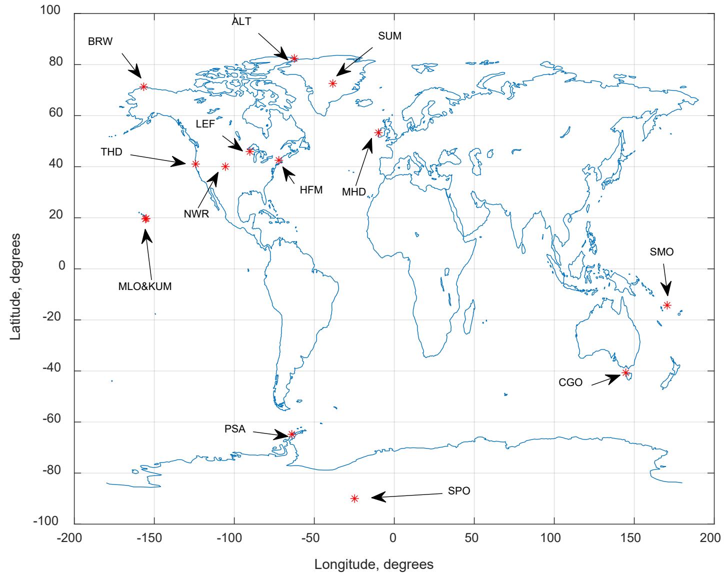

Figure 1. Location of the 14 NOAA stations considered in this work

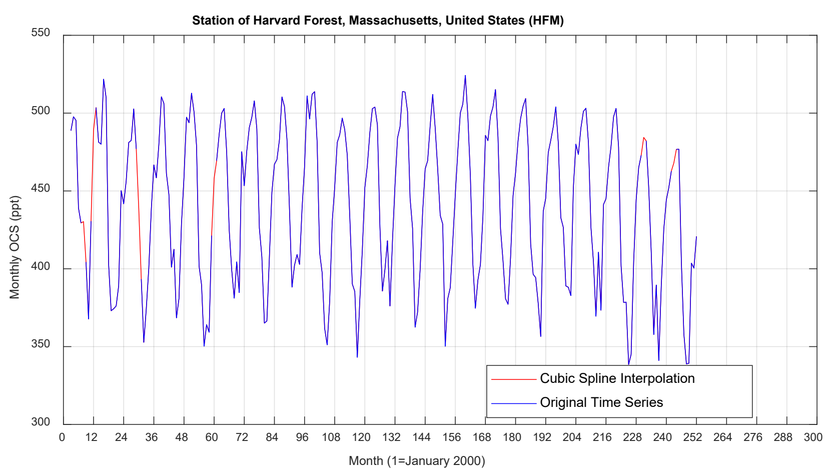

Figure 2. Example of a monthly OCS time series showing the gap-filling with cubic spline interpolation. The case shown in the figure refers to the HFM station.

2.2. Methods: trends identification

The long-term behaviours or trends in data are identified through the empirical mode decomposition (EMD) technique, developed to process nonlinear and nonstationary data (Huang et al., 1998) and successfully applied in many different fields, e.g., (Capparelli et al., 2013; Coughlin & Tung, 2004; Echeverría et al., 2001; Laurenza et al., 2012; Lee & Ouarda, 2011, 2012; Loh, 2004; Y. Wu & Shen, 2016). EMD decomposes a time series into a finite number of intrinsic mode functions (IMFs) and a residual by using an adaptive basis derived from the time series through a so-called “sifting” process, namely,

$$X(t) = \sum_{j=1}^{m} c_j(t) + r(t) \qquad (1)$$

where t is the time, *m* the number of modes, and $X(t)$ denotes a generic time series; c_j is j-th IMF, and finally, r is the residual, which can be either the *mean* trend or a constant. Because the series X is sampled at discrete time $t = j\Delta t, j = 1, \dots, N$, with N the total number of discrete measurements, we have that the whole time span of the series is $N\Delta t$. In our case, $\Delta t =1$ month. Furthermore, to simplify notation, hereafter, we will write j for $j\Delta t$ and N for $N\Delta t$.

In conventional trend analysis, it is often assumed, e.g., that the trend is linear, and therefore, it can be extracted with formal regression analysis (e.g. Gardiner et al., 2008; Lejeune et al., 2017). Furthermore, in non-parametric methods, the trend is analyzed through digital filtering techniques, e.g., the Fourier transform and low-pass filters to smooth the selected data and separate the low-frequency components from the seasonal cycle (e.g. Thoning et al., 1989).

In the present analysis, the trend is defined by considering all the components of the signal which show frequency modes lower than a given threshold frequency f_{th}; in this study, the default value is $f_{th} = 3/N$, that is the frequency corresponding to a period equal to $N/3$. Because in our analysis, the OCS time series is 17 to 20 years long, $N/3$ yields approximately 5–7 years. The threshold has been selected by trial and error and has been checked to provide a consistent analysis for the various stations. Also, OCS has a tropospheric lifetime of ~2–7 years (Blake, 2004), therefore frequencies lower than f_{th} characterizes long-term behaviour with timescales longer than the finite lifetime of OCS.

With this in mind, the trend, τ is defined according to,

$$\tau(t) = \sum_{j=l}^{m} c_j(t) + r(t) \qquad (2)$$

with $f_m < \cdots . < f_l \le f_{th}$. Again, this definition is consistent with the idea that the trend has to capture the low-frequency variability of the signal.

The characteristic frequency of a given mode, $c_j(t)$ can be identified with the usual computation of the classical Fourier variance spectrum analysis or Power Spectral Density (PSD). Later in this study (see section 3.2), we will show examples of how the frequency components within each IMF can be analyzed through the Hilbert transform (Huang et al., 1998). However, in case we are interested in determining the dominant frequency of each mode, we can resort to the classical PSD.

This work uses the EMD algorithm included in Matlab distribution 2020b, which implements all prescriptions and stopping criteria, as suggested by (Wang et al., 2010), to avoid the decomposition to run endlessly toward the limit with many infinite iterations of sifting, e.g., (Z. Wu & Huang, 2010). However, the black-box usage of the tool is not recommended. Even with the stopping criteria, there is no way to prevent the code from decomposing part of the trend in the lower frequency modes. Therefore there are at least three aspects that need to be carefully addressed when using the Matlab software package: a) how to fix the number of modes, m; b) how to prevent mode splitting and mode mixing; c) how to handle problems with the boundaries or end effects because of the finiteness of the series.

For issue a), we limit the number of modes to m=4, which is based on physical insights. We know that the observations are affected by noise; therefore, the first mode will fit the high oscillatory component of the noise. The second IMF or mode is expected to fit the annual cycle. The third is devoted to representing inter-annual variability, which is likely to be found in the series. Finally, the fourth last mode is to model possible lower frequency oscillations and, therefore, long-term trend structures. For this reason, by default, we have the threshold criterion $f_{th} = 3/N$ in defining the trend: everything with frequency lower than $f_{th} = 3/N$ is moved to the trend. The threshold f_{th} can be changed in case we are interested in looking at EMD reconstruction of the signal, which includes specific frequencies.

For issue b), we use the EEMD (Ensemble Empirical Mode Decomposition, e.g., (Z. Wu & Huang, 2009)) strategy of adding noise to the observations. For a given sample of observations, $X(j), j = 1, \dots, N$ we build up the noise sample $\tilde{X}(j) = X(j) + w(j)$, with w a Gaussian noise term with zero mean and standard deviation, σ_w. $\tilde{X}(j)$ is EMD decomposed, and the operation is repeated $nsamples$ time. Finally, the four IMF and the residual are taken by considering the average over the corresponding $nsamples$. However, before performing EMD on $\tilde{X}(j)$, we first extend the signal to account for possible boundary effects.

To this end, - issue c) -, we use the strategy proposed by (Stallone et al., 2020). The series $\tilde{X}(j)$ is symmetrically extended outside the boundaries, producing, on both sides, an extended signal $\tilde{X}_{ext}(j)$ which is, on each side, N times longer than the original one. Then, $\tilde{X}_{ext}(j)$ is multiplied by a function $\chi(j)$, which is one for the original signal $\tilde{X}(j)$ and tends smoothly to zero as we approach the two left and right ends of the extended signal. In this way, the signal $\tilde{X}_{ext}(j)$ is periodic at the boundaries.

For completeness, the last word has to be said for σ_w. We know that the observation noise of the OCS measurement is below 2 ppt or less than 0.5% on average. Therefore, σ_w is taken equal to 1.5 ppt to preserve the original structure of the series.

For the benefit of the reader, we summarize the algorithm we have devised to apply EMD to the OCS time series.

1. Set $f_{th} = 3/N$ (default value, $3/N$) and σ_w(default value, =1.5 ppt)
2. Set the maximum number of modes (default, $m = 4$)
3. Set the number of random samples, (default, $nsamples = 1000$)
4. Generate the noisy series $\tilde{X}(j), j = 1, \dots, N$
5. Generate the extended series $\tilde{X}_{ext}(j), j = 1, \dots, 3N$
6. EMD the series $\tilde{X}_{ext}(j)$
7. Store the IMFs and the residual over the original range of the signal, $j = N + 1, \dots, 2N$
8. Repeat steps 4 to 7 $nsamples$ times
9. Compute the final IMFs and residual by considering the average over the $nsamples$ of the corresponding functions calculated at step 7.

10. Compute the pdf or power density function of the four IMF (we use the tool $pcov$ in the Matlab distribution 2020b).
11. Compute the frequency peak of each IMF and related uncertainty
12. Compute the trend according to Eq. (2).

It should be stressed that the above procedure has been finalized, and the sensitivity of the procedure to the various parameters checked by trial and error, simulations, and applications to the time series at hand.

To explain how the EMD decomposition is applied and used in this study, we show its application to the MLO series (monthly averages from March 2000 to December 2020 ($N = 250$ months). The decomposition consists of 4 modes, and a residual and is shown in Fig. 3, and it is possible to see that the higher mode numbers are associated with lower frequency variability.

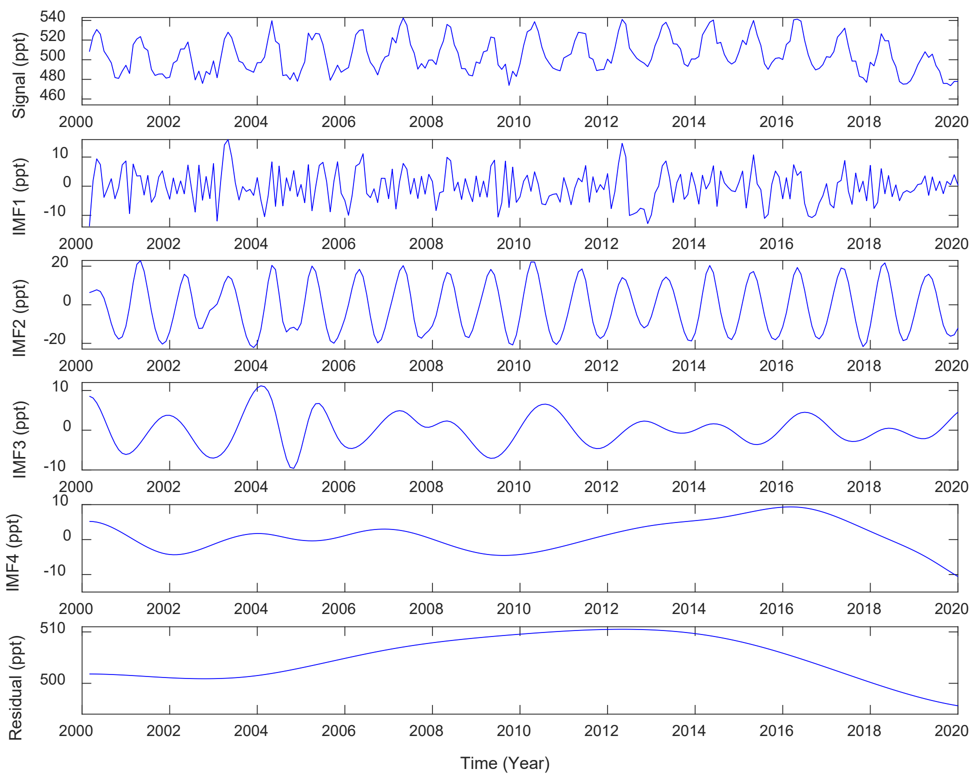

Figure 3. Exemplifying the EMD analysis applied to MLO monthly mean mole fractions measured for OCS (in ppt). Top to bottom, signal, IMFs and residual.

As expected, the first IMF extracts the high oscillatory component of the noise. The second component is an almost perfect harmonic of the constant period, although the amplitude can change with time. To better understand the relevant frequencies in the third and fourth modes, the PDFs of the four IMFs in Fig. 3 are shown in Fig. 4.

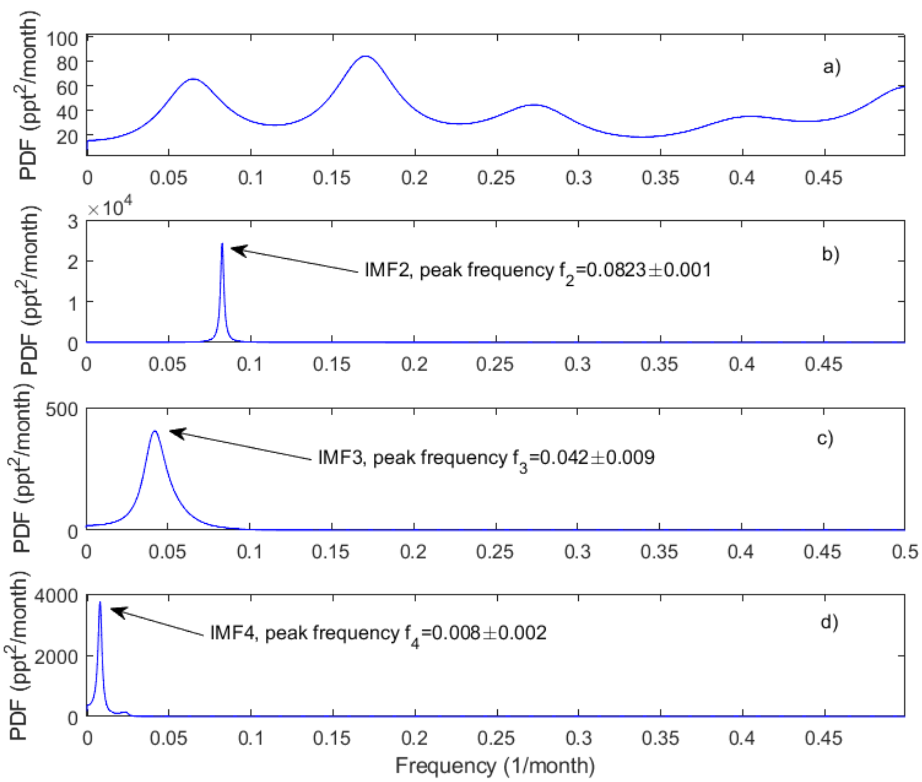

Figure 4. MLO station. Power density functions of the four IMF corresponding to the EMD decomposition of the MLO monthly time series; a) IMF1; b) IMF2; 3) IMF3; d) IMF4. The figure also shows the peak frequency of IMF2-4.

From Fig. 4, we see that the first IMF has a flat spectrum as expected for white noise, and its spectral density is two orders of magnitude lower than the sharp power of the annual cycle (there is a ratio 100:1 in the y-axis scale of IMF2 vs IMF1). Compared with Fig. 3, it is possible to see that the EMD methodology can filter out the random component in the data.

The second IMF extracted from the MLO record yields a frequency peak almost exactly at $1/12 \cong 0.0833$ in units of 1/month. IMF2 has the most prominent spectral density, and in fact, from Fig. 3, we see that the mode is close to a pure harmonic with a period equal to 12 months. We also see that the amplitude is not exactly the same from year-to-year, suggesting the presence of interannual variability. To perform an assessment of how close IMF2 is to a pure harmonic, we have fitted it with the model

$$A sin\left(\frac{2\pi(t-\tau)}{T}\right) \qquad (3)$$

with the time t in units of months and $T = 12$ months; the amplitude and delay A, τ are fit parameters. A Least Squares fitting procedure of the model of Eq. (3) to the IMF2 data shown in Fig. 3 (to phase the harmonic with the calendar year, the fit considers the data from January 2001, ($t = 1$) up to December 2020 ($t = 240$)) yields, $A = 17.27$ ppt, with a 95% confidence interval of $[16.51, 18.03]$ ppt and, $\tau = 1.93$ months, with a 95% confidence interval of $[1.85, 2.02]$ months.

The goodness of the fit has been assessed through the correlation coefficient, and we found $R^2 = 0.90$. The delay $\tau \sim 2$ months says that the peak value is attained in May, whereas the trough is in November. Finally, on average, the annual cycle's peak-to-peak amplitude is equal to ~ 34 ppt in the MLO measurement record.

The third IMF is close to 2 years, although its uncertainty is as large as ~6 months, and its spectral density is 1-2 order of magnitude lower than that of the annual cycle. However, although of less intensity, the IMF3 power maximizes at a value which is in good agreement with the QBO (Quasi Biennal Oscillation) mean cycle, which has a periodicity of 28-29 months, or ~0.4 per year, e.g., see (Ray et al., 2020). Finally, the fourth mode is more peaked than the third. It has a larger density but corresponds to a period close to 10 years. Therefore this mode is moved to the trend or long-term behaviour, which is shown in Fig. 5. In passing, we note that the frequency uncertainty shown in Fig. 4 is computed as the Half-Width at Half-maximum of the corresponding spectral line.

According to the definition of Eq. (2), the EMD trend, τ is prescribed to show time scales larger than those corresponding to the threshold frequency, $f_{th} = 3/N$, which for the MLO station corresponds to $\sim$ seven years. From Fig. 5 we see that on time scales larger than 7 years, the decline of the OCS in recent years is clearly seen. Again in Fig. 5, the EMD trend is compared with the other two smoothing, non-parametric and non-linear, algorithms. These are the *lowess,* τ_l (an acronym of locally weighted scatter plot smoothing, e.g., (Cleveland and Devlin, 1988) and the moving average, τ_{ma}. They are both prescribed with a span of $N/3$ to properly compare with the time scales designed for the EMD trend. The *lowess* smoothing is based on a local least-squares fitting and generalizes the smoothing average method, which is also shown in Fig. 5. It is seen that the moving average filter shows a high-frequency ringing close to the boundaries of the signal, where it tends to collapse on the data points. In contrast, the *lowess,* τ_l is much more consistent at the boundaries, although it provides a smoother version than the EMD, τ. Nevertheless, the comparison exemplifies how EMD yields a methodology to determine and control the characteristic scales we want to include in the reconstruction of the signal.

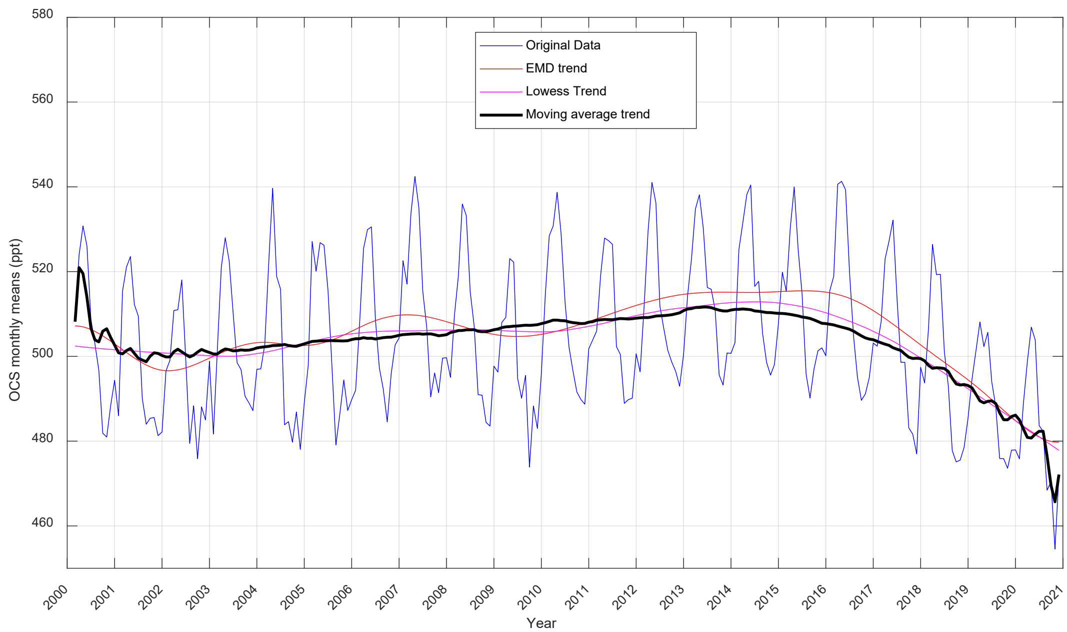

Figure 5. OCS monthly averages (2000 to 2020) for the MLO station and trend analysis according to EMD, lowess and moving average filters (e.g., see Eq. (2) and the text in the paper).

To exemplify this aspect, Fig. 6 provides a reconstruction of the signal, which also includes the IMF3. Therefore, this is equivalent to using a threshold $f_{th} = 1/12$, in order to remove the annual cycle from the original data. Based on the pdf analysis in Fig. 4, the EMD reconstruction in Fig. 6 includes all characteristics scales larger than ~ 2 years. For comparison, Fig. 6 also shows the representation of the data after their smoothing with a moving average filter with a span of 12, 24, and 36 months, respectively. From Fig. 6, we see that the moving average still retains a high oscillatory component, likely due to the observation noise. Conversely, EMD reconstruction appears smoother because the noise has been filtered through the IMF1, which is not included in the reconstruction. EMD clearly identifies the very large peak-to-peak variation across 2004-2005 and the relative trough in 2009-2010. These features are attenuated in the moving average filters. Finally, the distance among peaks of the EMD reconstruction suggests variability scales of 2 – 4 years, which, as discussed above, could be linked to QBO.

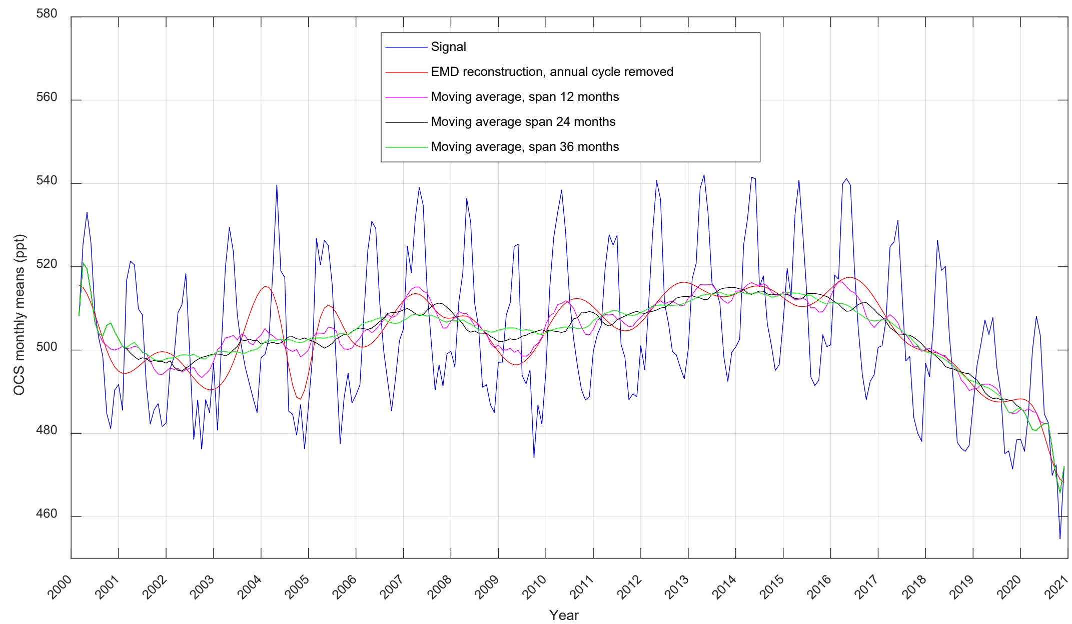

Figure 6. OCS monthly averages (2000 to 2020) for the MLO station and trend analysis according to the EMD reconstruction with the removal of the annual cycle. For comparison, the figure also shows the results with a moving average filter with three different time spans, 12, 24 and 36 months, respectively.

Before closing this section, we also note that a conventional Fourier analysis of the signal does not detect all of the modes evidenced for OCS by the EMD analysis. Figure 7 shows the PDF of the MLO time series, whose EMD composition has been exemplified through Fig. 3 to Fig. 4. It is seen that the Fourier analysis is capable of extracting the annual cycle. In contrast, the remaining modes, which EMD identifies in Fig. 3, are lost in a broad low pass spectrum with a zero-frequency peak. Figure 7 also shows, for comparison, the PDF of the second IMF, which extracts the annual cycle from the original signal. It can be seen that the PDF of the second IMF exactly matches the peak of the annual cycle in the PDF signal, which allows us to stress the property of EMD to extract the relevant modes from the signal. An analysis based solely on the PDF of the signal would conclude the presence of a single dominant mode and a low-pass component with a peak at zero frequency, which parallels the EMD residue and IMF4. In contrast, EMD can correctly identify the annual cycle but can also reveal cyclic mode in the lower frequency range with a characteristic time of ~10 years (IMF4). In addition, EMD reveals an intermediate mode that can be linked to inter-annual variability of characteristic time scales of 2-3 years, which, in turn, may be associated with influences from the QBO, e.g. (Ray et al., 2020).

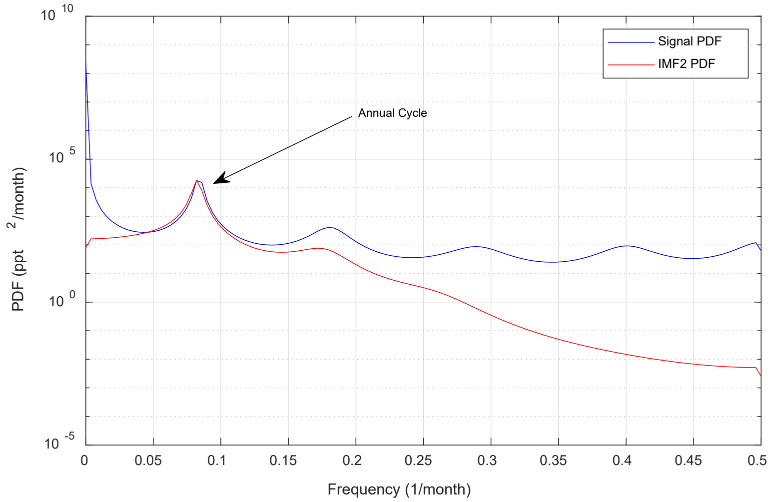

Figure 7. Power Density Function of the whole signal derived from a Fourier analysis of the MLO OCS monthly mean mole fraction time series over the past 20 years ("Signal PDF"), and the second IMF extracted through the EMD analysis.

3. Results for the NOAA network: OCS measurements for the year range 2000-2020

3.1. The long-term EMD component, τ

The OCS monthly mole fraction time series from the NOAA and cooperative sampling stations listed in Tab. 1 has been processed to identify EMD analysis trends computed according to Eq. (2). The EMD trend, τ, results for the North-Hemisphere stations north of 30°N are shown in Fig. 8. The EMD τ yields the long-range behaviour with frequency lower than the threshold $f_{th} = 3/N$. The decomposition is shown in Fig. 8. All Northern stations consistently show a decreasing atmospheric OCS mole fraction from 2015-2020.

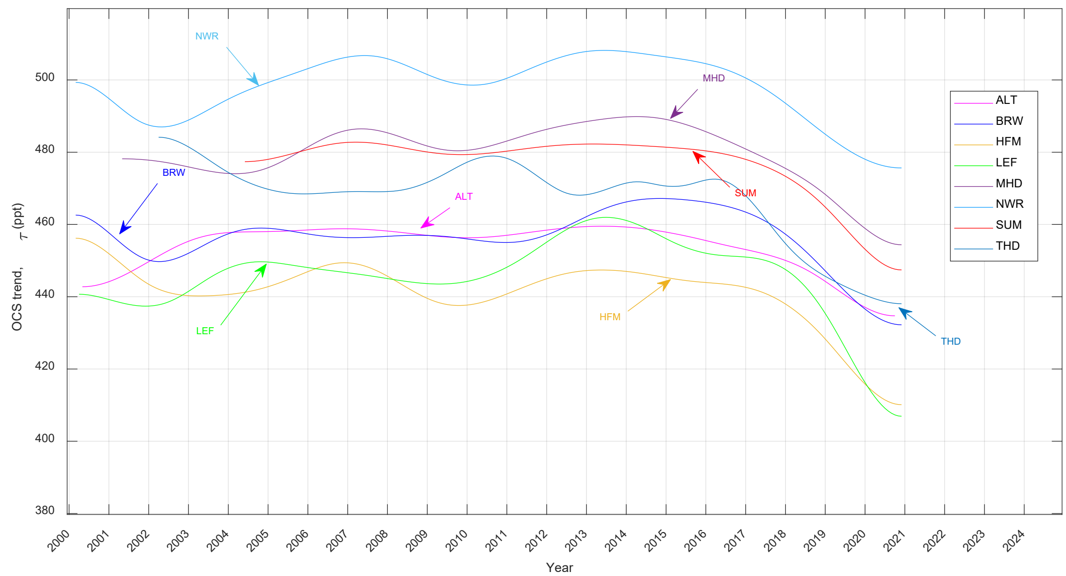

Figure 8. EMD-derived trend determination, τ component (Eq. (2)), for the NOAA stations in the Northern Hemisphere at latitudes greater than 30N.

The long-term component is always relevant in terms of explained variance, as shown in Tab. 2. In terms of standard deviation, the trend τ explains more than ~15% of the variability of the whole signal, $X(j), j = 1, \ldots, N$. We stress that the long-term components' variability in Fig. 8 reflects a good general agreement with original data. The overall mean is not distorted and long-term local features at the scale of the threshold frequency are well reproduced. This is exemplified in Fig. 9 for the case of the NWR station. In Fig. 9 we also show a comparison with the *lowess* trend, τ_l, which as for the case of the MLO station smooths the features at the scale of the threshold frequency, $f_{th} = 3/N$. For the sake of brevity, the comparison between $\tau$and τ_l is not shown in the paper for all stations. However, the supplemental material has provided this comparison for the interested reader. Here we stress that the *lowess* smoothing agrees with EMD in detecting a decline in OCS atmospheric column amount since 2015-2016.

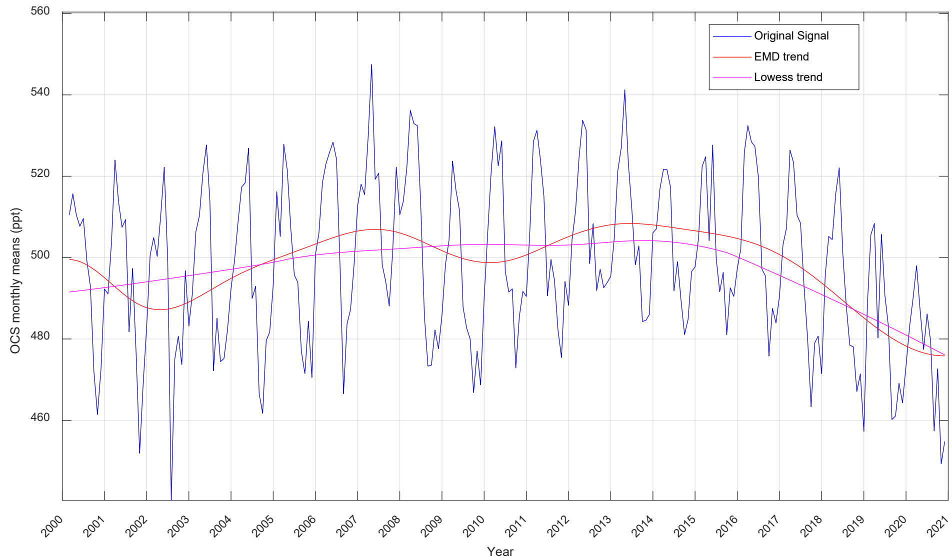

Figure 9. OCS monthly averages (2000 to 2020) for the NWR station and trend analysis according to EMD (Eq. (2) and the non-parametric *lowess* approach (see text in the paper).

The results for the stations between 30N and 30S are shown in Fig. 10. Consistent with what has been shown for the Northern Hemisphere, we see a decreasing trend for the three stations since 2015-2016.

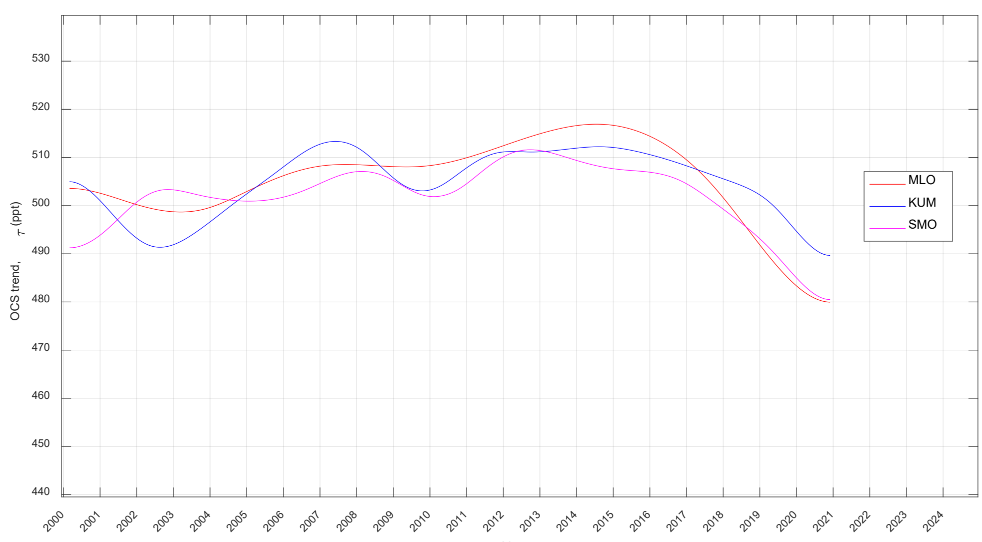

Figure 10. EMD-derived trend determination, τ component (Eq. (2)) for the NOAA stations between 30°N and 30°S.

Finally, Fig. 11 shows the results for the three stations in the Southern Hemisphere. Also in this case, we have that the three stations show a negative trend since 2015-2016, which is strongly consistent with the findings we have shown for the other NOAA stations after these years.

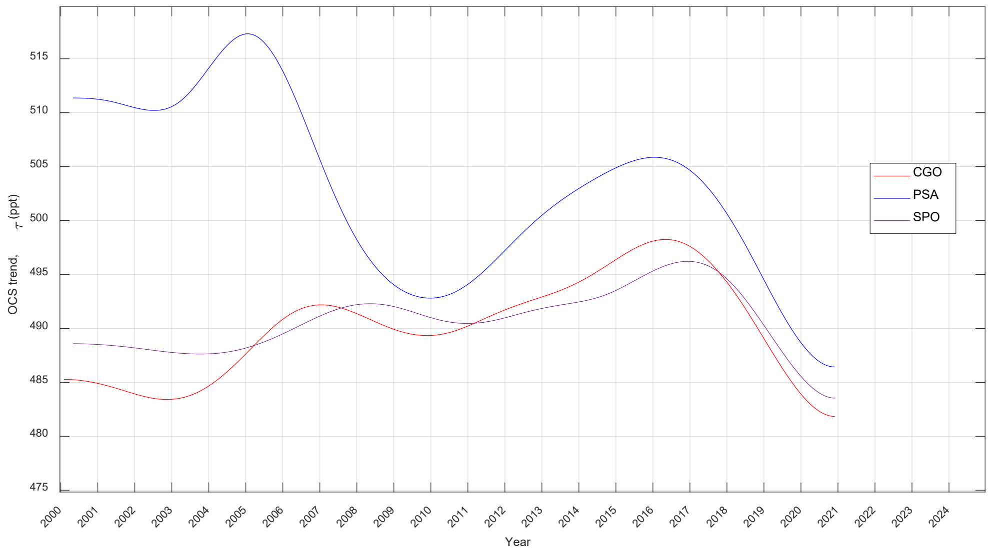

Figure 11. Trend analysis for the NOAA stations in the Southern Hemisphere. We note that for PSA, the trend seems to have reversed from a decreasing one since about 2010. However, it is likely that the trend at PSA may be influenced by contamination in sampling equipment used at that site in the first half of the record (2000-2010). The record is certainly quite a bit noisier prior to 2010 than after it.

An essential aspect of the analysis we have shown with the 20-year long time series is the presence of a relatively large variance of the OCS signal at frequencies below the threshold $f_{th} = \frac{3}{N}$ which may reflect scales of the general atmospheric circulation, the climate forcing or even the long-term changes in the magnitude of overall or total OCS emissions, e.g, (Zumkehr et al., 2018).

The low-frequency variability is shown in Tab. 2 in terms of the standard deviation, i.e., the variability strength, of the EMD trend τ (computed according to Eq. (2)) and the original monthly observations, $X(j), j = 1, \ldots, N$.

Table 2. *Variability (in terms of standard deviation) of the EMD trend τ (Eq. (2)) and the original signal, $X(j), j = 1, \ldots, N$, for the 20 year-long time series analyzed in this paper.*

Station	Code	Lat [°N]	Lon [°W]	Elevation [masl]	Variability [ppt]		
					Trend, τ	Signal, $X(j)$	% Ratio Trend/Signal
Alert, Nunavut, Canada	ALT	82.4508	62.5072	185	5.38	39.64	13.6
Point Barrow, USA	BRW	71.3230	156.6114	11	6.34	40.87	15.5
Cape Grim, Tasmania	CGO	-40.683	144.6900	94	4.26	14.76	28.8
Harvard Forest, USA	HFM	42.5378	72.1714	340	8.34	49.53	16.8
Cape Kumukahi, USA	KUM	19.7371	155.0116	0.30	6.10	22.48	27.1
Park Falls, USA	LEF	45.9451	90.2732	472	9.62	44.77	21.4
Mace Head, Ireland	MHD	53.3260	9.899	5.00	7.00	33.35	20.9

Mauna Loa, USA	MLO	19.5362	155.5763	3397	6.98	17.90	38.9
Niwot Ridge, USA	NWR	40.0531	105.5864	3523	7.65	19.91	38.4
Palmer Station, Antarctica	PSA	-64.7742	64.0527	10	8.52	20.03	42.5
Tutuila, American Samoa	SMO	-14.2474	170.5644	42	5.80	12.85	45.1
South Pole, Antarctica	SPO	-89.98	24.8	2810	2.65	14.69	6.40
Summit, Greenland	SUM	72.5962	38.422	3209	8.24	34.19	24.1
Trinidad Head, USA	THD	41.0541	124.151	107	9.95	41.40	24.0

From Tab. 2, we see that the trend or long-term variability is in between ~15-40% of the total power of the signal. Therefore, this component is not negligible with respect to the yearly cycle. In effect, from Fig.s 8-11, we see that the variability has consistently increased in the last few years, which leads us to conclude that the OCS mole fraction has entered a worldwide phase of decline. These findings suggest a recent broad-scale atmospheric decline that is captured by measurements at all of the NOAA sites.

In conclusion, we can say that the twenty-year OCS record at all sites shows a consistent low-frequency component, which yields a complex behaviour with a generally increasing trend up to 2015, a temporary decrease during 2009, and finally a decline in the last 6-7 years.

3.2. Oscillatory modes

Although this study focuses mainly on assessing low-frequency components in NOAA's OCS records over the past twenty years, EMD also extracts other relevant modes in the time series. Throughout the paper, we have already noticed the strong presence of the annual cycle, which is due to the summer OCS drawdown by vegetation. However, EMD analysis has also revealed modes of frequency $>\frac{3}{N}$. In principle, this rich variability could be associated with climate characteristic scales such as the QBO ($\sim$2 years), (El-Nino ($\sim 2-7$ years), or simply interannual variability linked to biogenic activities. The in-depth analysis of these modes is not the present study's focus. However, we highlight them here for the benefit of the reader and to incite further studies. The peak frequencies of the IMF 2 to 4 are shown in Fig. 12 as a function of the station. From Fig. 11, we see a great consistency among the various stations. The IMF2 represents the annual cycle, with frequency $f_o = \frac{1}{12} = 0.0833$ month^{-1}, and we see that IMF2 at all stations is peaked at this frequency. In Fig. 11, we have also drawn the sub-tone frequency, $f_o/2$, $f_o/4$ and $f_o/10$ to help to identify where the observed peak frequencies accumulate.

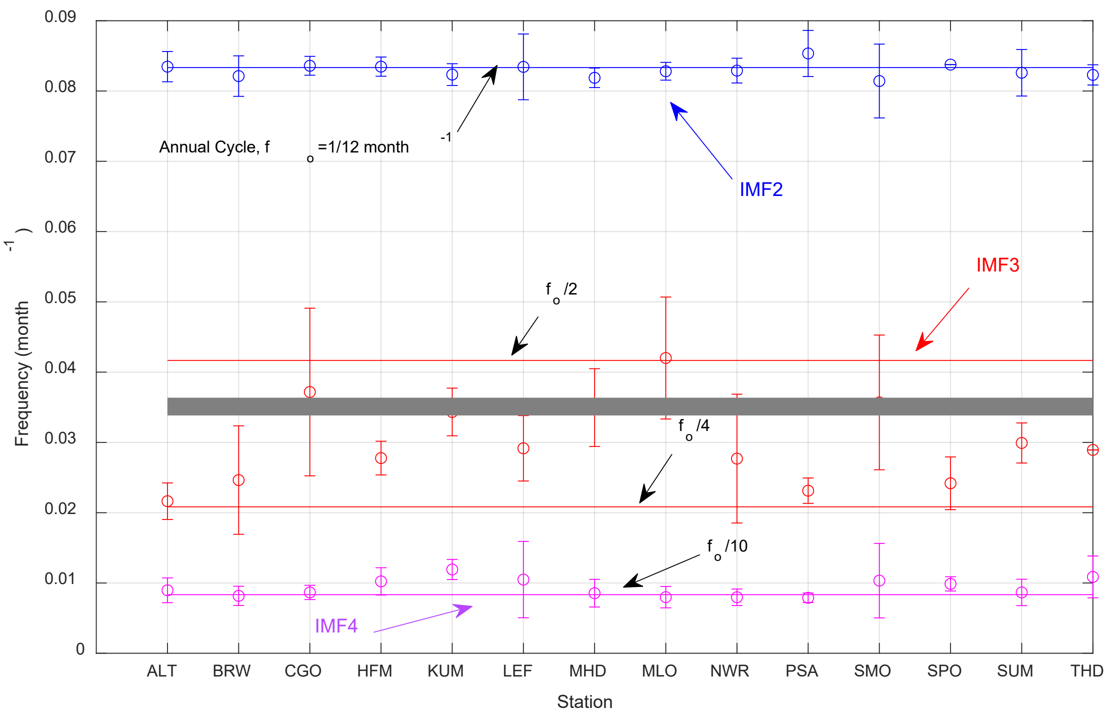

Figure 12. Peak frequencies of the IMF from 2 to 4 as a function of the station. The figure also shows the subtone frequencies of the annual cycle f_o, that is $f_o/2$, $f_o/4$ and $f_o/10$ to identify where the observed peak frequencies accumulate. The grey area gives the range of the QBO mean cycle, which has a periodicity of 28-29 months.

It is seen that the IMF4 tends to accumulate at the frequency $f_o/10$, which is lower than the threshold frequency, f_{th}. In effect, the IMF4 has been moved to the trend τ, according to its definition of Eq. (2). Much more interesting is the behavior of the IMF3. This is the faintest among the three shown in Fig. 11 and shows good consistency with the QBO mean cycle, potentially related to its influence on atmospheric mixing processes (Ray et al., 2020), or on the natural the balance of OCS sources and sinks. The presence of this frequency within the range $f_o/4$, $f_o/2$ is consistent with the IMF3 being linked to QBO.

Before ending this section, we also show examples of the Huang-Hilbert transforms or *hht* used to check for time-dependence of the frequency. The transform is exemplified in Fig. 13 for the second mode or IMF2 related to the EMD decomposition of the MLO OCS time series. The transform gives the frequency as a function of the time (expressed in months in Fig. 12), and each (t, f) pair has assigned an instantaneous strength or amplitude (in ppt) according to the color bar. In the case of a pure sine wave of frequency, $A\,sin(2\pi f t)$, the *hht* would give a flat line equal to f and a constant amplitude equal to A. To clarify the meaning of the transform, in Fig. 13 we also show the flat line corresponding to the annual cycle, that is 1/12 month^{-1}

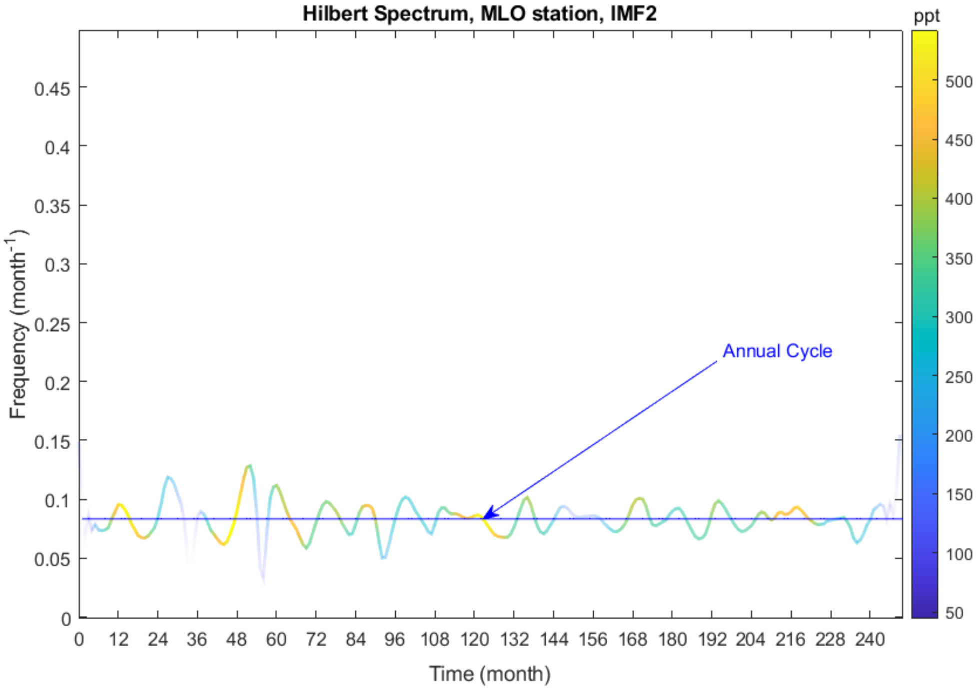

Figure 13. The plot shows the *hht* transform which represents the instantaneous frequency spectrum of the IMF2 component decomposed from the original mixed signal for the MLO station. For comparison, the plot also shows the line corresponding to the annual cycle.

We see that the frequency oscillates around the annual cycle, showing that just one dominant harmonic governs the time dependence of IMF2. For IMF3, see Fig. 14, we have that the intensity of the amplitude is fainter and again is close to the peak frequency. For IMF3, we see an amplitude increase around 2005 (~58 months in Fig. 14). The frequency tends to increase, and in fact, if we go back to Fig. 3, it appears that around 2005, the frequency of the oscillations of the 3rd mode tends to increase. However, for IMF3 the hht transform is close to the frequency 0.042 1/month, computed with the PDF analysis shown in Fig. 4.

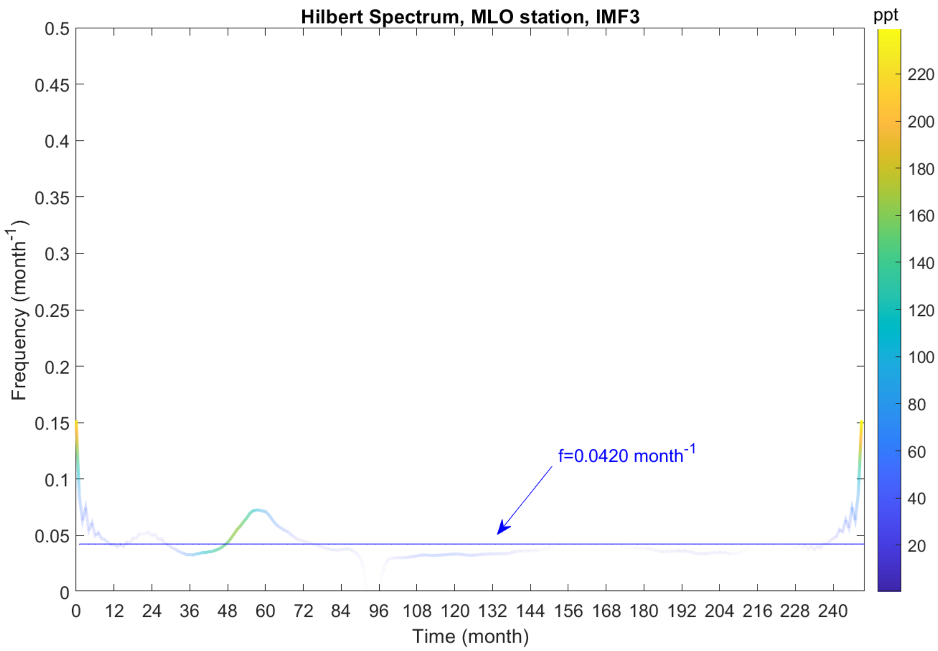

Figure 14. As Fig. 12 but for IMF3. For comparison, the plot also shows the flat line corresponding to frequency 0.042 month^{-1}, which the PDF analysis has extracted from the mode IMF3.

Note that the slight bump we see at around 2005 (month 58) is a transient phenomenon, which seems to relax back to a stationary behaviour in a time span of the basic period of 1 year.

4. Discussion and Conclusions

In this study, monthly average time series of OCS have been analyzed using data from the NOAA/GML network covering 2000 to 2020. The analysis has been performed by using the Empirical Mode Decomposition, which decomposes a given time series in its primary cycles plus a trend. The method is non-parametric, and there is no need to specify a trend model as generally done with other approaches.

EMD is more suitable than traditional methods for the analysis of nonlinear and nonstationary signals. However, the straightforward applications of the technique could lead to misuse if its known limitations and basic assumptions are not carefully considered. EMD still has some open issues about its formal characterization when operating on a broadband signal, such as white noise, e.g., (Z. Wu & Huang, 2010). In our analysis, this issue has been minimized by resorting to decomposition, which, while non-exact, still provides an approximation of the given signal (Wang et al., 2010). The EMD method we use to calculate the decomposition has been implemented with the two basic stopping criteria recommended by (Wang et al., 2010) *to obtain physically meaningful results.* The stopping rules include a Cauchy criterion, e.g., (Wang et al., 2010) to stop the iteration from getting a given IMF and an Energy ratio criterion, e.g., (Wang et al., 2010) to stop the EMD decomposition. In this way, as stressed by (Wang et al., 2010), the EMD implementation yields an approximation with respect to the cubic spline basis but avoids resulting in IMFs that have no physical significance.

In addition, we remark that other problems could affect EMD performance in practice (Huang et al., 1998, 2003), especially in measurement noise. One limitation is the difficulty of carrying out a clean separation in IMFs when their local frequencies are too close, e.g., (Stallone et al., 2020). In some cases, this separation could be improved by applying the so-called Ensemble Empirical Mode Decomposition (EEMD) (Z. Wu & Huang, 2009), an approach taken in this paper, which adds random noise the observations.
Finally, we constrain EMD by specifying the maximum number of modes and a frequency threshold to separate lower frequencies from the annual cycle. In effect, the stopping criteria (Wang et al., 2010) embedded in the most updated EMD software tool by Matlab (we used the release 2020b in this study) do not provide a reliable strategy to separate the trend from pure modes. Therefore, we have shown that frequency thresholding and a suitable limitation of modes are *best practices* for the successful use of Empirical Mode Decomposition.

With this in mind, the decomposition in cyclic modes of the OCS series has shown the presence of low-frequency time scales of ~ 10 years. Furthermore, the low-frequency component yields a long-range time evolution, indicating a decline in OCS concentration in the atmosphere in the last 6-7 years. The reduction is seen in data obtained from all stations examined in the present work, consistent with a recent imbalance in total global OCS sources and losses. Moreover, we have shown that the OCS records exhibit a cyclic mode between 2-4 years, which may be linked to the Quasi Biennal Oscillation (QBO)).

In conclusion. a decreasing trend of OCS mole fraction has been observed in the last 6-7 years at all NOAA/GML measurement sites. No matter the origin of the present OCS decay, the carbonyl sulfide atmospheric budget is currently unbalanced. We think that further analysis with global transport models could yield new insights in light of these most recent changes that we have identified and assessed in this study.

Acknowledgments

Measurements from flasks from the fourteen stations listed in Tab. 1 have been downloaded from the website http://www.esrl.noaa.gov/gmd/hats/gases/OCS.html. We give credit to the National Oceanic and Atmospheric Administration (NOAA)/Global Monitoring Laboratory (GML) in Boulder as a source of the data and appreciate the technical assistance of B. Hall, C. Siso, and I. Vimont, for assisting with the creation and maintenance of a reliable long-term atmospheric history of OCS mole fraction. This research was carried out in the framework of the project `OT4CLIMA' which was funded by the Italian Ministry of Education, University and Research (D.D. 2261 del 6.9.2018, PON R&I 2014-2020 and FSC).

Open Research

The OCS data used in the paper are freely available from the website http://www.esrl.noaa.gov/gmd/hats/gases/OCS.html.

References

Aydin, M., Britten, G. L., Montzka, S. A., Buizert, C., Primeau, F., Petrenko, V., et al. (2020). Anthropogenic Impacts on Atmospheric Carbonyl Sulfide Since the 19th Century Inferred From Polar Firn Air and Ice Core Measurements. *Journal of Geophysical Research: Atmospheres*, *125*(16). https://doi.org/10.1029/2020JD033074

Berry, J., Wolf, A., Campbell, J. E., Baker, I., Blake, N., Blake, D., et al. (2013). A coupled model of the global cycles of carbonyl sulfide and CO_2 : A possible new window on the carbon cycle. *Journal of Geophysical Research: Biogeosciences*, *118*(2), 842–852. https://doi.org/10.1002/jgrg.20068

Blake, N. J. (2004). Carbonyl sulfide and carbon disulfide: Large-scale distributions over the western Pacific and emissions from Asia during TRACE-P. *Journal of Geophysical Research*, *109*(D15), D15S05. https://doi.org/10.1029/2003JD004259

Brühl, C., Lelieveld, J., Crutzen, P. J., & Tost, H. (2012). The role of carbonyl sulphide as a source of stratospheric sulphate aerosol and its impact on climate. *Atmospheric Chemistry and Physics*, *12*(3), 1239–1253. https://doi.org/10.5194/acp-12-1239-2012

Campbell, J. E., Carmichael, G. R., Chai, T., Mena-Carrasco, M., Tang, Y., Blake, D. R., et al. (2008). Photosynthetic Control of Atmospheric Carbonyl Sulfide During the Growing Season. *Science*, *322*(5904), 1085–1088. https://doi.org/10.1126/science.1164015

Campbell, J. E., Whelan, M. E., Seibt, U., Smith, S. J., Berry, J. A., & Hilton, T. W. (2015). Atmospheric carbonyl sulfide sources from anthropogenic activity: Implications for carbon cycle constraints. *Geophysical Research Letters*, *42*(8), 3004–3010. https://doi.org/10.1002/2015GL063445

Campbell, J. E., Berry, J. A., Seibt, U., Smith, S. J., Montzka, S. A., Launois, T., et al. (2017). Large historical growth in global terrestrial gross primary production. *Nature*, *544*(7648), 84–87. https://doi.org/10.1038/nature22030

Camy-Peyret, C., Liuzzi, G., Masiello, G., Serio, C., Venafra, S., & Montzka, S. A. (2017). Assessment of IASI capability for retrieving carbonyl sulphide (OCS). *Journal of Quantitative Spectroscopy and Radiative Transfer*, *201*, 197–208. https://doi.org/10.1016/j.jqsrt.2017.07.006

Capparelli, V., Franzke, C., Vecchio, A., Freeman, M. P., Watkins, N. W., & Carbone, V. (2013). A spatiotemporal analysis of U.S. station temperature trends over the last century: On the Temperature Trends over the United States. *Journal of Geophysical Research: Atmospheres*, *118*(14), 7427–7434. https://doi.org/10.1002/jgrd.50551

Coughlin, K. T., & Tung, K. K. (2004). 11-Year solar cycle in the stratosphere extracted by the empirical mode decomposition method. *Advances in Space Research*, *34*(2), 323–329. https://doi.org/10.1016/j.asr.2003.02.045

Echeverría, J. C., Crowe, J. A., Woolfson, M. S., & Hayes-Gill, B. R. (2001). Application of empirical mode decomposition to heart rate variability analysis. *Medical & Biological Engineering & Computing*, *39*(4), 471–479. https://doi.org/10.1007/BF02345370

Gardiner, T., Forbes, A., de Mazière, M., Vigouroux, C., Mahieu, E., Demoulin, P., et al. (2008). Trend analysis of greenhouse gases over Europe measured by a network of ground-based remote FTIR instruments. *Atmospheric Chemistry and Physics*, *8*(22), 6719–6727. https://doi.org/10.5194/acp-8-6719-2008

Glatthor, N., Höpfner, M., Baker, I. T., Berry, J., Campbell, J. E., Kawa, S. R., et al. (2015). Tropical sources and sinks of carbonyl sulfide observed from space: TROPICAL

SOURCES AND SINKS OF COS. *Geophysical Research Letters*, *42*(22), 10,082-10,090. https://doi.org/10.1002/2015GL066293

Huang, N. E., Shen, Z., Long, S. R., Wu, M. C., Shih, H. H., Zheng, Q., et al. (1998). The empirical mode decomposition and the Hilbert spectrum for nonlinear and non-stationary time series analysis. *Proceedings of the Royal Society of London. Series A: Mathematical, Physical and Engineering Sciences*, *454*(1971), 903–995. https://doi.org/10.1098/rspa.1998.0193

Huang, N. E., Wu, M.-L. C., Long, S. R., Shen, S. S. P., Qu, W., Gloersen, P., & Fan, K. L. (2003). A confidence limit for the empirical mode decomposition and Hilbert spectral analysis. *Proceedings of the Royal Society of London. Series A: Mathematical, Physical and Engineering Sciences*, *459*(2037), 2317–2345. https://doi.org/10.1098/rspa.2003.1123

Kettle, A. J. (2002). Global budget of atmospheric carbonyl sulfide: Temporal and spatial variations of the dominant sources and sinks. *Journal of Geophysical Research*, *107*(D22), 4658. https://doi.org/10.1029/2002JD002187

Krysztofiak, G., Té, Y. V., Catoire, V., Berthet, G., Toon, G. C., Jégou, F., et al. (2015). Carbonyl Sulphide (OCS) Variability with Latitude in the Atmosphere. *Atmosphere-Ocean*, *53*(1), 89–101. https://doi.org/10.1080/07055900.2013.876609

Laurenza, M., Vecchio, A., Storini, M., & Carbone, V. (2012). Quasi-Biennal Modulation of Galactic Cosmic Rays. *The Astrophysical Journal*, *749*(2), 167. https://doi.org/10.1088/0004-637X/749/2/167

Lee, T., & Ouarda, T. B. M. J. (2011). Prediction of climate nonstationary oscillation processes with empirical mode decomposition. *Journal of Geophysical Research*, *116*(D6), D06107. https://doi.org/10.1029/2010JD015142

Lee, T., & Ouarda, T. B. M. J. (2012). Stochastic simulation of nonstationary oscillation hydroclimatic processes using empirical mode decomposition: Simulation of NSO Using EMD. *Water Resources Research*, *48*(2). https://doi.org/10.1029/2011WR010660

Lejeune, B., Mahieu, E., Vollmer, M. K., Reimann, S., Bernath, P. F., Boone, C. D., et al. (2017). Optimized approach to retrieve information on atmospheric carbonyl sulfide (OCS) above the Jungfraujoch station and change in its abundance since 1995. *Journal of Quantitative Spectroscopy and Radiative Transfer*, *186*, 81–95. https://doi.org/10.1016/j.jqsrt.2016.06.001

Loh, C.-H. (2004). Application of the Empirical Mode Decomposition-Hilbert Spectrum Method to Identify Near-Fault Ground-Motion Characteristics and Structural Responses. *Bulletin of the Seismological Society of America*, *91*(5), 1339–1357. https://doi.org/10.1785/0120000715

Maseyk, K., Berry, J. A., Billesbach, D., Campbell, J. E., Torn, M. S., Zahniser, M., & Seibt, U. (2014). Sources and sinks of carbonyl sulfide in an agricultural field in the Southern Great Plains. *Proceedings of the National Academy of Sciences*, *111*(25), 9064–9069. https://doi.org/10.1073/pnas.1319132111

Montzka, S. A., Calvert, P., Hall, B. D., Elkins, J. W., Conway, T. J., Tans, P. P., & Sweeney, C. (2007). On the global distribution, seasonality, and budget of atmospheric carbonyl sulfide (COS) and some similarities to CO_2. *Journal of Geophysical Research*, *112*(D9), D09302. https://doi.org/10.1029/2006JD007665

Ogée, J., Sauze, J., Kesselmeier, J., Genty, B., Van Diest, H., Launois, T., & Wingate, L. (2016). A new mechanistic framework to predict OCS fluxes from soils. *Biogeosciences*, *13*(8), 2221–2240. https://doi.org/10.5194/bg-13-2221-2016

Ray, E. A., Portmann, R. W., Yu, P., Daniel, J., Montzka, S. A., Dutton, G. S., et al. (2020). The influence of the stratospheric Quasi-Biennial Oscillation on trace gas levels at the Earth's surface. *Nature Geoscience*, *13*(1), 22–27. https://doi.org/10.1038/s41561-019-0507-3

Stallone, A., Cicone, A., & Materassi, M. (2020). New insights and best practices for the successful use of Empirical Mode Decomposition, Iterative Filtering and derived algorithms. *Scientific Reports*, *10*(1), 15161. https://doi.org/10.1038/s41598-020-72193-2

Thoning, K. W., Tans, P. P., & Komhyr, W. D. (1989). Atmospheric carbon dioxide at Mauna Loa Observatory: 2. Analysis of the NOAA GMCC data, 1974-1985. *Journal of Geophysical Research: Atmospheres*, *94*(D6), 8549–8565. https://doi.org/10.1029/JD094iD06p08549

Wang, G., Chen, X.-Y., Qiao, F.-L., Wu, Z., & Huang, N. E. (2010). On Intrinsic Mode Function. *Advances in Adaptive Data Analysis*, *02*(03), 277–293. https://doi.org/10.1142/S1793536910000549

Whelan, M. E., Lennartz, S. T., Gimeno, T. E., Wehr, R., Wohlfahrt, G., Wang, Y., et al. (2018). Reviews and syntheses: Carbonyl sulfide as a multi-scale tracer for carbon and water cycles. *Biogeosciences*, *15*(12), 3625–3657. https://doi.org/10.5194/bg-15-3625-2018

Wu, Y., & Shen, B.-W. (2016). An Evaluation of the Parallel Ensemble Empirical Mode Decomposition Method in Revealing the Role of Downscaling Processes Associated with African Easterly Waves in Tropical Cyclone Genesis. *Journal of Atmospheric and Oceanic Technology*, *33*(8), 1611–1628. https://doi.org/10.1175/JTECH-D-15-0257.1

Wu, Z., & Huang, N. E. (2009). Ensemble Empirical Mode Decomposition: A Noise-Assisted Data Analysis Method. *Advances in Adaptive Data Analysis*, *01*(01), 1–41. https://doi.org/10.1142/S1793536909000047

Wu, Z., & Huang, N. E. (2010). On the Filtering Properties of the Empirical Mode Decomposition. *Advances in Adaptive Data Analysis*, *02*(04), 397–414. https://doi.org/10.1142/S1793536910000604